Research Article

Fluorescence Sensor Based on Polyaniline Supported Ag-ZnO Nanocomposite for Malathion Detection

Sintayehu Berhanu [1], **Fikradis Habtamu,**[1] **Yordanos Tadesse,**[2] **Fantahun Gonfa,**[1] **and Tesfaye Tadesse**[1]

[1]*Department of Chemistry, Bonga University, Bonga, P.O. Box 334, Bonga, Ethiopia*
[2]*Department of Chemistry, Salale University, Fiche, P.O. Box 245, Fiche, Ethiopia*

Correspondence should be addressed to Sintayehu Berhanu; sintayehuberhanu38@gmail.com

Sensitive and selective determination of harmful organophosphate is rigorously fundamental due to its large negative influence on the environment and human health. Ultrasensitive fluorescence nanocomposite was developed for malathion detection which was based on electrostatic interaction between polyaniline and Ag-ZnO nanocomposite. The nanocomposite (Ag-ZnO/PANI) was prepared via the sol-gel technique next in situ oxidative polymerization of polyaniline. The synthesized nanocomposite was characterized by FT-IR, XRD, SEM, UV-vis, and fluorescence spectroscopic techniques. The fluorescence intensity of the nanocomposite was quenched by MA, which was proportional to the concentration of MA in the range of 0–1000 nM, with a detection limit of 13.2 nM. The proposed method was sensitive, selective, easy in design, and fast in operation. Therefore, it has been effectively used for MA detection in agricultural products with suitable recovery.

1. Introduction

Organophosphate pesticides (OPs) have been utilized worldwide because of their particular benefits such as ease of synthesis, low environmental persistence, and the moderately high death rate for insects [1, 2]. Inferable from their persistence, toxicity, and bioaccumulation, they make long-term harm to the environment and living species [3, 4]. Specifically, malathion (MA) is an organophosphate pesticide which is mainly used to enhance food production and control pests and increases harvest all over the world. However, unreasonable use of OPs results in various adverse effects on human beings, wildlife, and the environment [4–6].

Consumption of agricultural products which contain excessive amounts of malathion could combine with certain cholinesterases (such as acetylcholinesterase (AChE)) in the human body, cause serious damage to human nerve function, and even cause unsteadiness, shortness of breath, cerebral pain, loss of motion, respiratory damages, aggravated asthma, and death [3–6]. Several methods have been developed over

the past few years for the determination of OPs, such as high-performance liquid chromatography [6], gas chromatography [7], enzyme-linked immune sorbent assays [8], colorimetric sensing [9], and fluorescence spectroscopy [1, 10–12].

These ordinary techniques are sensitive and accurate, but they suffer from numerous drawbacks, including substantial instruments, time-consuming processes, significant expense, long analysis time, the necessity of highly trained personnel, and the inability to be used for continuous monitoring [13]. Recently, the OP pesticide biosensors advanced to AChE inhibition. Furthermore, biocompatible nanomaterials in biosensors improve their performance by augmenting the surface area needed for AChE immobilization as well as reducing the response time [14].

Conversely, measurements based on the quenching of the photoluminescent characteristics of nanomaterials have been widely used for the detection of DNA, proteins, microorganisms, metal ions, and others. It has different advantages such as high sensitivity and selectivity, fast response time, visualization, and being inexpensive and accurate for

qualitative and quantitative detection of Ops [1, 5]. Considering the previous works, enzyme-free sensors based on metals or their oxides like CuO [15], CeO_2 [16], Fe_2O_3 [17], MnO_2 [18], and others have been utilized due to their minimal expense, excellent electrocatalytic activity, and the capacity to conduct electrochemical reactions at lower potentials [15–18].

Zinc oxide (ZnO) is perhaps the most encouraging material in sensory applications because of its high conductive electron movement and great adsorption quality [19]. However, limitations like low sensitivity, poor selectivity, and high working temperature are as yet difficulties related to these sensors [20]. To beat the drawback and to upgrade the detecting characteristics, the modification supported by different metals and organic molecules has drawn extensive interest [19–24].

There are several reports on the upgrading of the electronic, catalytic, and sensorial potential of ZnO by incorporating noble metals such as Cu, Pt, Co, Pd, and Ag [21, 25, 26]. Among these, Ag merits special consideration due to its stability, conductivity, nontoxic nature, and comparatively less expensive. The incorporation of Ag nanoparticles (NPs) with ZnO in the polymer matrix upgrades the mechanical properties and modifies the surface and conductivity of ZnO [21, 26]. Polyaniline (PANI) is also an important polymer with high conductivity and an extensional conjugated electron framework. Supporting the inorganic filler with this organic polymer is used to tune the optical, electrical, and photocatalyst properties as well as upgrade the detecting capability of ZnO [25, 27].

Subsequently, in the present study, Ag-decorated ZnO supported by PANI (Ag-ZnO/PANI) NCs was synthesized. The NC crystalline size, morphological properties, optoelectronic properties, and surface functional groups were characterized by X-ray diffraction, scanning electron microscope, UV-vis, and FT-IR techniques. The sensitivity and selectivity of the NCs to MA were studied by using a fluorescence spectrophotometer.

2. Experimental Methods

2.1. Reagents and Chemicals.
Silver nitrate (169.87 g/mol), Zinc(II) acetate dehydrate (183.48 g/mol), aniline (93.13 g/mol), sulphuric acid (98 g/mol), sodium hydroxide (40 g/mol), oxalic acid (90.03 g/mol), hydrochloric acid (36.46 g/mol), ethanol (46.07 g/mol), ammonium persulfate (228.18 g/mol), and malathion (330.358 g/mol) were used. All chemicals were of analytical grade (Sigma-Aldrich) and used as received without further purification.

2.2. Synthesis of Ag-ZnO Nanoparticle.
Silver-doped zinc oxide (Ag-doped ZnO) NPs were prepared by a sol-gel method [28]. 100 mmol of Zn(II) acetate dehydrate was dissolved in 200 mL of ethanol solution and stirred for 30 min. Separately, oxalic acid dehydrate (55.8 mmol) was dissolved in 80 mL of ethanol solution which was added slowly with constant stirring for 3 hr to the Zn(II) acetate solution until a white solution was formed. To this solution, 4% wt of silver nitrate was added and stirred for an additional 3 hr. The solution was dried on a water bath to form a xerogel. The xerogel was calcined at 500°C in a muffle furnace at a heating rate of 5°C/min. Then, it was kept at this temperature for 2 hr, lastly obtaining a dark brown powder of Ag-ZnO after grinding using the motor pestle.

2.3. Synthesis of Ag-ZnO/PANI Nanocomposite.
The synthesis of Ag-ZnO/PANI NCs was carried out as follows: 2 g of Ag-ZnO NPs were added into 200 mL of 1 M H_2SO_4 solution. 2 mL of aniline was added dropwise to the solution and stirred for 30 min until a silvery-white color was formed. A solution of 35.1 mmol of ammonium persulfate oxidant in 100 mL of H_2SO_4 solution was added dropwise under a refrigerator and stirred for 30 min. The solution color was changed into dark green confirming the formation of the Ag-ZnO/polyaniline hybrid.

It was kept at room temperature for 24 hr, and then, the solution was filtered and washed with distilled water until the filtrate became colorless. Finally, the precipitated material was filtered and dried in a vacuum oven at 80°C for 6 hours. Thus, Ag-ZnO/PANI NC was prepared [29, 30].

2.4. Structural Characterizations.
X-ray diffraction patterns were obtained using a BRUKER D8 (West Germany) and equipped with Cu Kα radiation ($\lambda = 1.5405$ Å) at room temperature in the scan range 2θ between 10 and 90°.

Accelerating voltage and the applied currents were 40 kV and 30 mA, respectively. The morphologies of the nanocomposites were done by using EVO 18 SEM. The absorbance was recorded by using the SPECTRONIC GENESYS 2PC UV-vis spectrophotometer. Fourier transform infrared (FT-IR) spectroscopy was used in the region between 4000 and $400 \, cm^{-1}$ to determine the functional groups and surface structure of the samples by a model of Shimadzu 8400S (German) using KBr plates. The fluorescence spectra were measured using Shimadzu RF 5301PC spectrofluorimeter.

2.5. Detection of MA and pH Optimization.
A stock solution of 50 mg/L of MA was prepared in 100 mL of double distilled and deionized water. Sensing of OPs was performed by preparing a series of concentrations and by adjusting the pH (7) to the optimum at room temperature. The MA sensing was performed by monitoring the fluorescence behavior of the Ag-ZnO supported by the PANI NC solution.

The synthesized NC was dispersed in distilled water, and the spectra were recorded at different excitation wavelengths from 350 to 430 nm with a gap of 10 nm before the addition of OPs. Then, the fluorescence intensity of the aqueous solution of the NC was measured with a consecutive addition of 0.01 M of MA at 380 nm. To calculate the analytical parameters, the slope of the calibration curve was used based on Equation (1) [31]:

$$I_0 - \frac{I}{I_0} = m[\text{MA}] + b, \tag{1}$$

where I_0 and I represent the fluorescence intensities of Ag-ZnO/PANI in the absence and presence of MA, m-slope, and b-intercept and [MA] is the concentration of MA. The

limit of detection (LOD) can be calculated using the equation of LOD =3SD/slope, where SD is the standard deviation of the calibration curve [24]. The quenching efficiency (QE) was estimated using Equation (2) [31].

$$QE = I_0 - \frac{I}{I_0}. \tag{2}$$

To optimize the experimental condition, the reaction times between the NCs and MA were investigated. Furthermore, the effect of pH was studied in the pH range of 3 to 11.

Each time, the pH was maintained by using 0.1 M HCl and 0.1 M NaOH measured by a pH meter under a constant excitation wavelength and concentration.

2.6. Detection of Real Sample. The methodology was applied for MA sensing from two different agricultural products (potatoes and tomatoes) which were purchased purposively from a local market. The samples were allowed to be dried, then grounded and spiked with MA standards of 0.05, 0.1, and 0.15 M and 0.25 μM, separately. Then, they were carefully standardized and formerly allowed to stand for 24 hr. The powders were mixed with 30 mL ethanol and 5 mL water, with ultrasonic extraction for 1 hr, and centrifuged for 30 min at 4000 rpm. The supernatant was transferred and evaporated at 50°C [32].

Finally, the fluorescence spectra of the NCs and the dry residue solution were measured in ultrapure water. The selectivity of this technique was studied by evaluation of fluorescence intensity using UV-vis spectra taken before and subsequent addition of a series of Mg^{2+}, glucose, CO_3^{2-}, Cl^-, and Cd^{2+} [30, 33].

3. Results and Discussion

3.1. Characterization of the Nanocomposite

3.1.1. FT-IR Spectra. FT-IR technique was used to determine the functional groups of PANI and Ag-ZnO. The peak at 608 cm^{-1} in Figure 1(b) is attributable to the metallic stretching of Ag-O, and the small peak centered at 609 cm^{-1} in Figure 1(a) is due to the Ag-O group revealing the existence of Ag. In addition, the bands at 492 cm^{-1} showed Zn–O bond observed. The presence of peaks due to ZnO and Ag confirms the effective interaction of their elements. All these effects indicated well incorporation as well as the presence of inorganic filler (Ag-ZnO nanoparticle) into the host matrix.

The absorption band of PANI has occurred at 1126 cm^{-1} which is due to stretching vibration of quinoid ring Figure 1(a). The peak at 3442 cm^{-1} is attributable to the free N–H vibrational stretching of the primary and secondary amine groups. Similarly, the peaks associated with the C-H and C-N stretching vibrations are located at 2932 and 1470 cm^{-1}, respectively. In addition, the peak at 1293 and 801 cm^{-1} corresponds to the C-N in-plane deformation and a =CH in-plane vibration of PANI Figure 1(b). Thus, from the FT-IR spectra, it is confirmed that the NPs existent in the macromolecular chain of PANI and aniline monomers
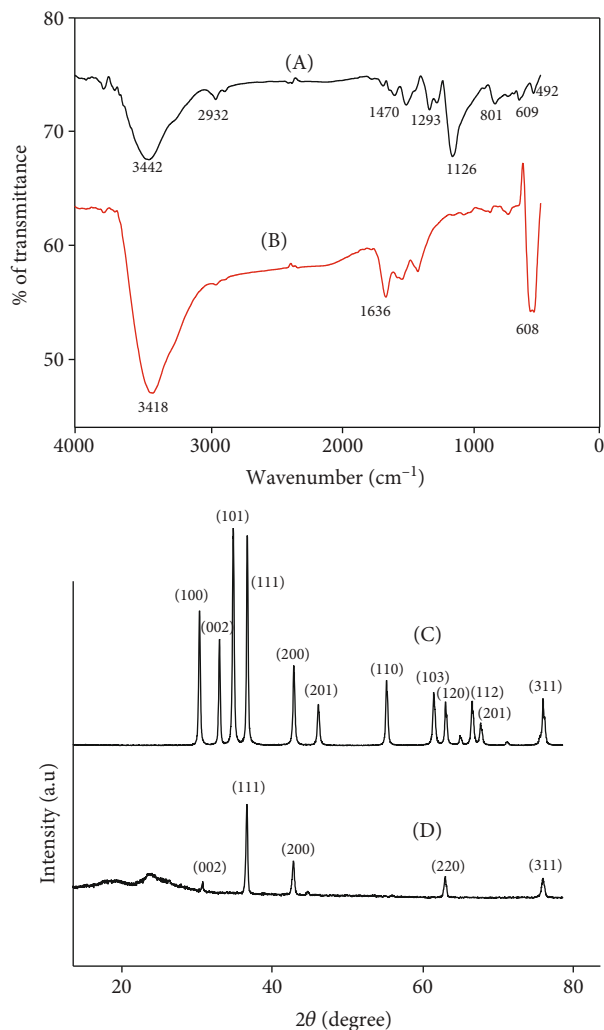

FIGURE 1: FT-IR spectra of Ag-ZnO/PANI (a) and Ag-ZnO (b); XRD patterns of Ag-ZnO (c) and Ag–ZnO/PANI NCs (d).

are successfully polymerized on the surface of Ag-ZnO NPs confirming that the PANI is existing in the NCs.

3.1.2. XRD Analysis. The XRD patterns of the Ag-ZnO and Ag-ZnO/PANI are shown in Figure 1. As shown in Figure 1(c), diffraction peaks located at 2θ = 31.79, 34.44, 36.27, 47.55, 62.87, 67.97, and 69.11° are in good agreement with (100), (002), (101), (102), (110), (103), (112), and (201) crystal plane of wurtzite structure of ZnO (JCPDS card.No.75-576).

The reflection planes at (111), (200), (120), and (311) show the characteristics of face-centered cube Ag metal in Ag-ZnO NPs (JCPDS, No. 04-0783). The average crystal grain size of Ag-ZnO NPs can be calculated according to the Scherrer equation (Equation (3)) [34], which estimated is as 35.68 nm [35, 36].

$$D_{hkl} = \frac{k\lambda}{\beta_{hkl}} \cos \theta_{hkl}, \tag{3}$$

where D_{hkl} is the particle size which is perpendicular to the

normal line of the plane ($k = 0.9$, $\lambda = 0.15405$ nm) (wavelength of X-ray), β_{hkl} is the FWHM of the diffraction line, and θ is the diffraction angle of hkl.

In the hybrid of Ag-ZnO/PANI, the diffraction peak of PANI was overlapped with the peak of Ag-ZnO, which results in a weak peak in the composite. The characteristic peaks corresponding to the reflection of (111), (200), (220), and (311) crystal planes were shown as 38.06, 44.23, 64.36, and 77.4°, respectively. It can be observed from Figure 1(d) that two broad amorphous peaks about $2\theta = 18°$ and 25.42° are related to the planes of the PANI molecular chain.

The average crystal size was calculated at 38.06, 44.23, and 64.36°, and the average size of the NCs estimated is about 31.52 nm. The diffraction peaks of Ag-ZnO NPS move slightly towards the direction of the 2θ decrease in the Ag-ZnO/PANI NCs, and there is variation in broadness and intensity which is due to the strong interfacial interaction among Ag-ZnO and the polymer of aniline [30, 35].

3.1.3. Morphology.
Morphological features of the as-synthesized Ag-ZnO and Ag-ZnO/PANI composites are shown in Figure 2. The Ag-ZnO NPs show an irregular morphology Figure 2(a) and ensure a certain extent agglomeration, which is because the radius of Zn is smaller than that of Ag, and the two NPs have different valence states. Consequently, there are some variations between them in morphology. Ag-ZnO/PANI NCs Figure 2(b) reveal that PANI is coated on the surface of Ag-ZnO, and the image showed an aggregate of particles with no distinct morphology, but brighter spots on the surfaces possibly represented Ag metal on the nanocomposite.

3.1.4. UV-vis Spectra.
UV-vis spectrum of PANI NPs is shown in Figure 3(a), and the characteristic band was observed at 415 and 310 nm with a bandgap of 2.73 eV. The absorption peak observed at this two-point is expected for aromatic nuclei with π-π * electronic transitions and charge transfer from the benzenoid ring to the quinoid rings [30]. The UV-vis spectrum of Ag NPs is shown in Figure 3(b) with a strong absorption peak of about 418 nm with a bandgap of 2.8 eV, which is attributed to the surface plasmon resonance, which confirms the symmetric and narrow size of Ag NPs [37].

The UV-vis spectra of Ag-ZnO and Ag-ZnO/PANI NC are presented and compared in Figures 3(c) and 3(d). The Ag-ZnO particles represent a sharp absorption peak around 430 nm corresponding to the bandgap of 2.61 eV, and the modification of the ZnO by Ag significantly affects the bandgap [31, 38]. As expected, the Ag-ZnO particles supported by PANI could expand the wavelength response to longer. The central absorption edge for Ag-ZnO/PANI rose at 470 nm, attributable to the 2.42 eV bandgap [30].

According to Rahman et al. [38], Ag-ZnO NPs exhibit lower bandgap energies compared to ZnO. It is observed that the characteristic peaks appear in Ag-ZnO/PANI NCs with a redshift in the peak position after the addition of PANI. This substantial increase in wavelength may be due to the interaction and synergism between Ag, ZnO, and PANI within NCs.

This can simplify the electron excitation with relatively low energy for enhanced detection of the malathion.

3.1.5. Photoluminescence Spectra.
The photoluminescence spectra of ZnO and Ag-ZnO NPs at excitation wavelengths of 360 and 370 nm are shown in Figures 3(e) and 3(f). Broad emission bands from 380 to 490 nm and 450 to 600 nm are shown for ZnO and Ag-ZnO NPs, respectively. To study the fluorescence properties of Ag-ZnO/PANI NCs, the emission spectra can be used to describe the recombination method of photogenerated holes and electrons by the fluorescence emission intensity. The good emission intensity is related to the recombination of photogenerated charge transporters with a short lifetime. The departure of the photogenerated transporter, holes, and electrons is large because of a longer lifetime, which allows weakening of the intensity in the fluorescence spectra [37]. The maximum emission fluorescence spectrum of Ag-ZnO/PANI NCs was obtained by exciting the NCs at the excitation wavelength of 380 nm (Figure 3(g)) with a range of 510-630 nm band centered at 581 nm.

3.2. Optimization of Experiments.
The stability of the sensor is fundamental; the effect of pH on fluorescence intensity in the presence of 1 μM MA solution is studied and carried out in the pH range of 3 to 11. Figure 4(a) shows that the change in pH of the solution had an observable change in the fluorescence intensity of the NCs and MA. The fluorescence had a maximum intensity at neutral pH (pH = 7). However, the fluorescence spectra of Ag-ZnO/PANI+MA are slowly declining again with further increasing or decreasing the pH from 7. This can be described depending on the protonation and deprotonation of the amine groups at the polyaniline surface and the carbonyl, sulfide, or methoxy group of MA.

It is stated that the benzenoid rings are the reason for the fluorescence emission, whereas at low pH the PANI is protonated and the quinoid rings act as a fluorescence quencher. Moreover, at low pH, the aggregation of Ag-ZnO/PANI is established by the action of intramolecular hydrogen bonds with the carbonyl, methoxy, or sulfide groups of MA on the surface of the Ag-ZnO/PANI+MA [31].

Moreover, at higher pH (8–11), the deprotonation of amino moieties of PANI has created a negative charge cloud on the surface and made anionic layers which undergo strong electrostatic interaction with different functional groups of MA. While at neutral pH there is no protonation or deprotonation of Ag-ZnO/PANI NC and MA, in addition, the maximum fluorescence is achieved. Therefore, we chose pH = 7 as the experimental condition.

Figure 4(b) illustrates the quenching efficiency of MA with increasing reaction time. Upon addition of 2 μM MA into the Ag-ZnO/PANI NC at pH 7, the fluorescence quenched quickly, and the fluorescence intensity nearly reached its lowest value after 30 sec depending on this result; the reaction time of 2 min seems to be selected for the detection of MA.

3.3. Quenching Mechanism of Sensor.
The most possible mechanism for the fluorescence enhancement of Ag-ZnO/
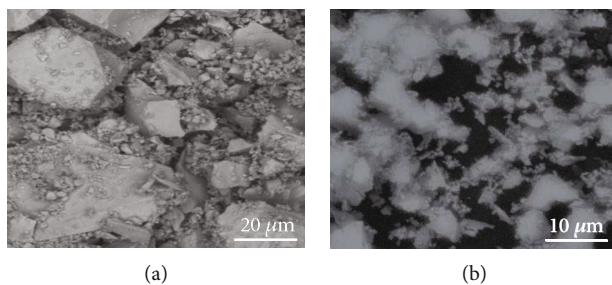
(a)　　　　　　　　　　　(b)

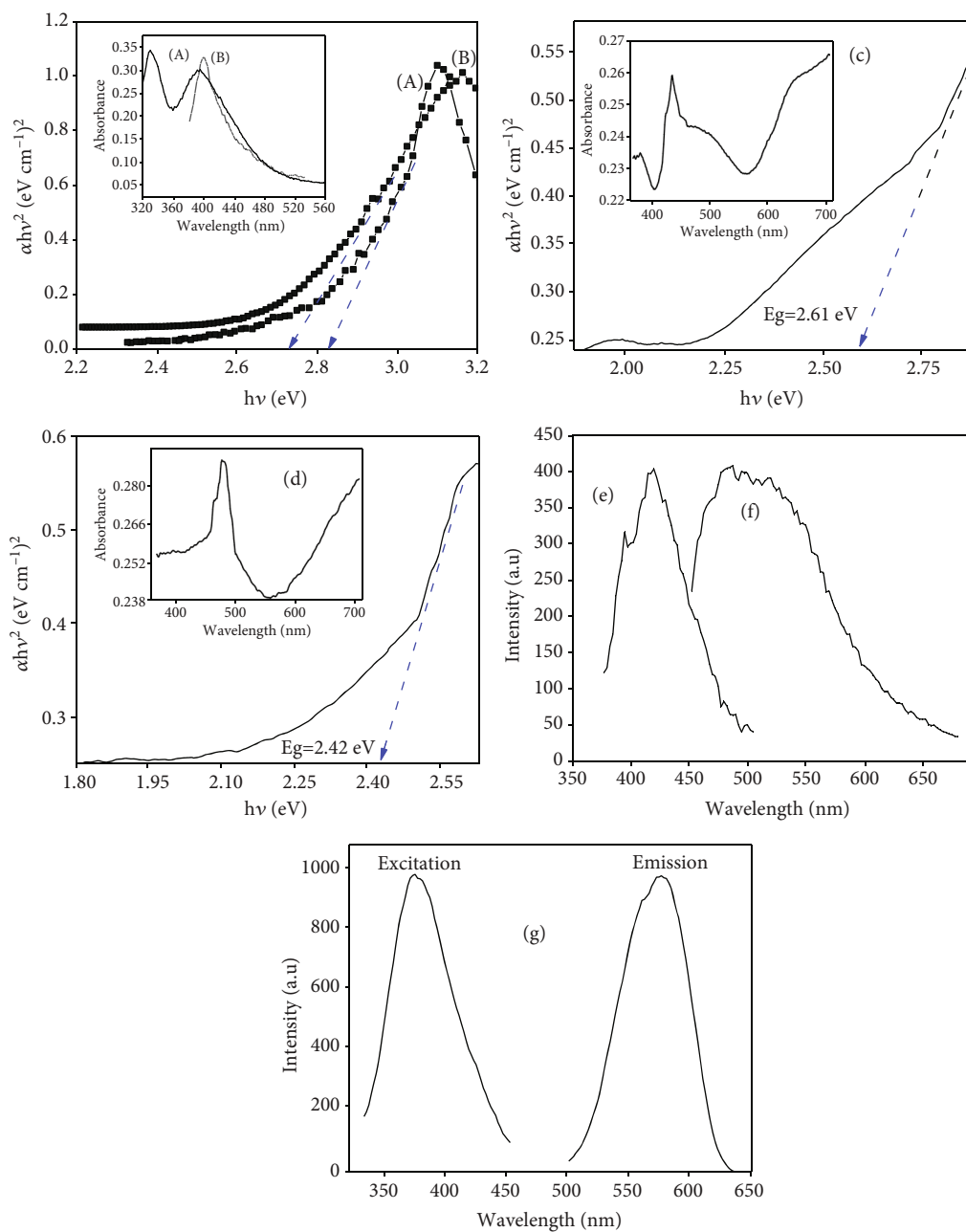FIGURE 2: SEM image of Ag-ZnO (a) and Ag-ZnO/PANI (b).

FIGURE 3: UV-vis absorption spectra of (a) PANI NPs, (b) ZnO NPs, (c) Ag-ZnO NPs, and (d) Ag-ZnO/PANI NCs and (e) fluorescence of ZnO NPs, (f) Ag-ZnO NPs, and (g) excitation and fluorescence emission spectrum of Ag-ZnO/PANI NCs.
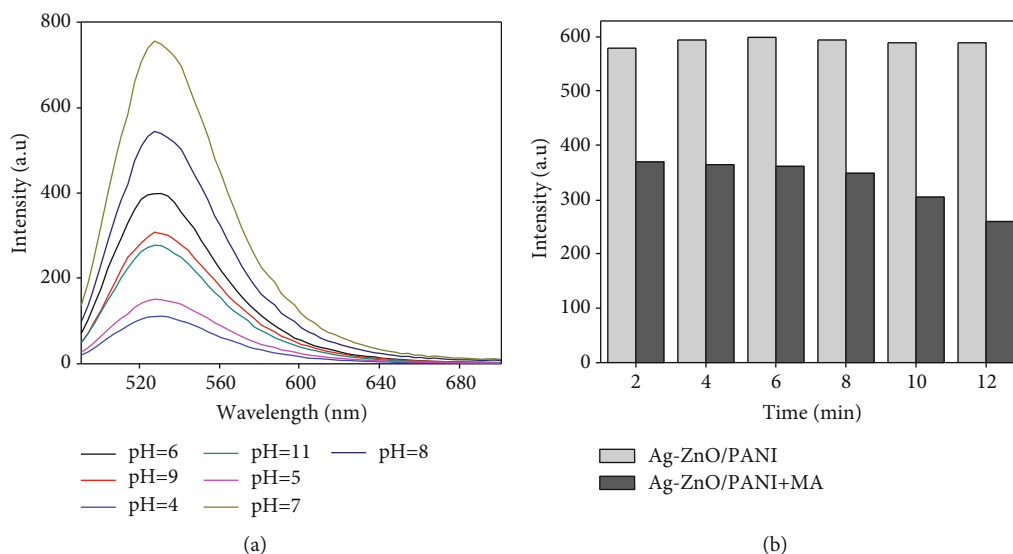
FIGURE 4: (a) Variation of fluorescent intensity in different pH of solutions using $1\,\mu$M of Ag-ZnO/PANI NCs and (b) the effect of reaction time on the fluorescence intensity of the Ag-ZnO/PANI + MA ($2\,\mu$M) at pH 7.
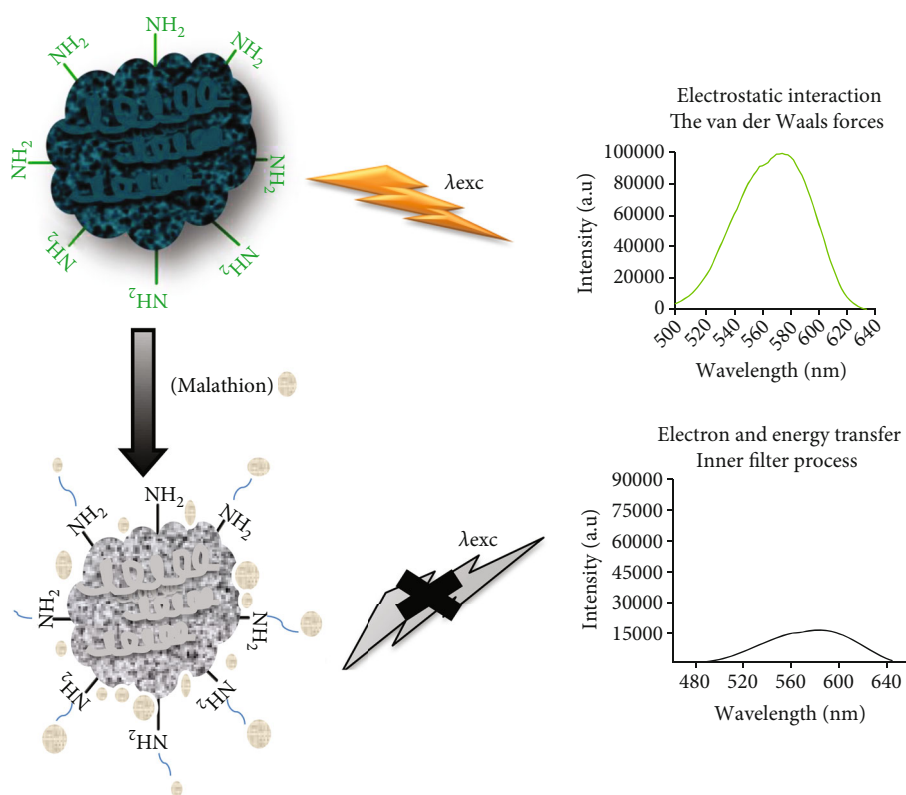

FIGURE 5: Schematic illustration of MA detection using Ag-ZnO/PANI NCs fluorescence sensor.

PANI NCS due to PANI adsorption onto Ag-ZnO NPs is based on the van der Waals force as well as the electrostatic force of interaction. A large number of delocalized electrons on the amine groups of PANI and the inorganic filler allow moderate electrostatic interaction. Such electrostatic effect is the main reason for the interaction between Ag-ZnO and PANI [39].

Generally, the quenching of the fluorescence spectra of Ag-ZnO/PANI NCs by MA is shown schematically in Figure 5, which possibly occur due to the inner filter process and electron and energy transfer. Inner filter effect needs an overlap
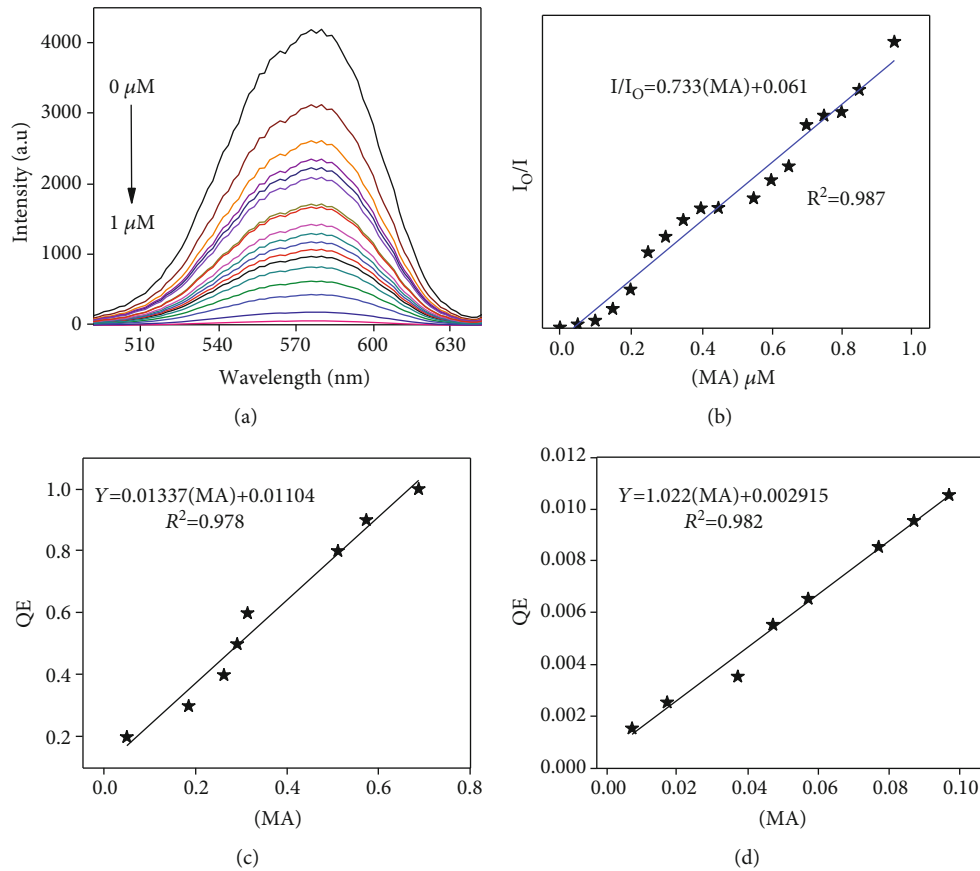
FIGURE 6: (a) Fluorescence quenching of Ag-ZnO/PANI NC with increasing concentrations of MA, (b) linear relationship plot representing Io/I and concentration of MA, I_o and I are the fluorescence intensities of Ag-ZnO/PANI nanocomposite in the absence and presence of MA, (c) QE versus MA concentration from 0.1 to 0.8 μM, and (d) from 0.01 to 0.1 μM at pH 7 and λex = 380 nm.

between the absorption spectrum of the MA, the excitation spectrum, and the emission band of the Ag-ZnO/PANI NC.

The absorption spectra of MA can be shielded as part of the radiation from the excitation of the Ag-ZnO/PANI NC, and the MA can absorb the emitted light by the Ag-ZnO/PANI NC. Additionally, the spectral overlap between the absorption peaks of MA and the absorption and emission spectra of Ag-ZnO/PANI NC allows the inner filter effect and subsequently reduces the intensity of the emission spectra.

Furthermore, the electron-donating amine groups of polyaniline can strongly interact with carbonyls as well as sulfide groups of MA. This effect is also told that the quenching mechanism is not associated only with the inner filter effect process but also forms the aggregate of the compound [30, 31, 37, 39, 40].

In the standard state, the fluorescence quantum yield (QY) of Ag-ZnO/PANI NCs was calculated relative to the integrated fluorescence emissions of L-tryptophan (standard solution of amino acids; QY = 0.1435) fluorescent with similar optical properties by using Equation (3) [41, 42].

$$\Phi_F = \Phi_{F(\text{std})} \times \frac{F \times A_{\text{std}} \times n^2}{F_{\text{std}} \times A \times n_{\text{std}}^2} \times \frac{F \times A_{\text{std}} \times n^2}{F_{\text{std}} \times A \times n_{\text{std}}^2}, \quad (4)$$

where F and F_{std} are the fluorescence area of the sample and the standard amino acid, respectively; A and A_{std} are the absorbance of the NCs and standard amino and; and n and n_{std} are the refraction index of the NCs and the standard amino acid. The QY of Ag-ZnO/PANI NCs is $0.149 \approx 15\%$. This value is approximately similar to the QY of the standard L-tryptophan that reported by Kirby and Steiner [43].

3.4. Sensitivity and Selectivity for MA.
The sensitivity of the sensor is one of the main aspects of analysis [44]. The intensity of the NC recovers proportionally with the concentration of malathion. To check the validity of this method, we used Ag-ZnO/PANI NC to detect MA in optimum conditions. An arrangement of MA solution composed of 0-1 μM together with an appropriate amount of Ag-ZnO/PANI NCs was used to measure the fluorescence spectra.

Fluorescence intensity of the maximal emission at 571 nm was observed, which varied with the concentration of MA Figure 6(a). The blue shift (~10 nm) observed revealed the formation of an aggregate of compounds. Although, the fluorescence intensity of the NPs decreased with increasing amounts of MA and the fluorescence quenching ratio was proportional to the MA concentration of 0.01-0.95 μM.

There are two linear regions of correlation in the MA concentration range of 0.01–0.1 μM ($R^2 = 0.990$) and 0.1–
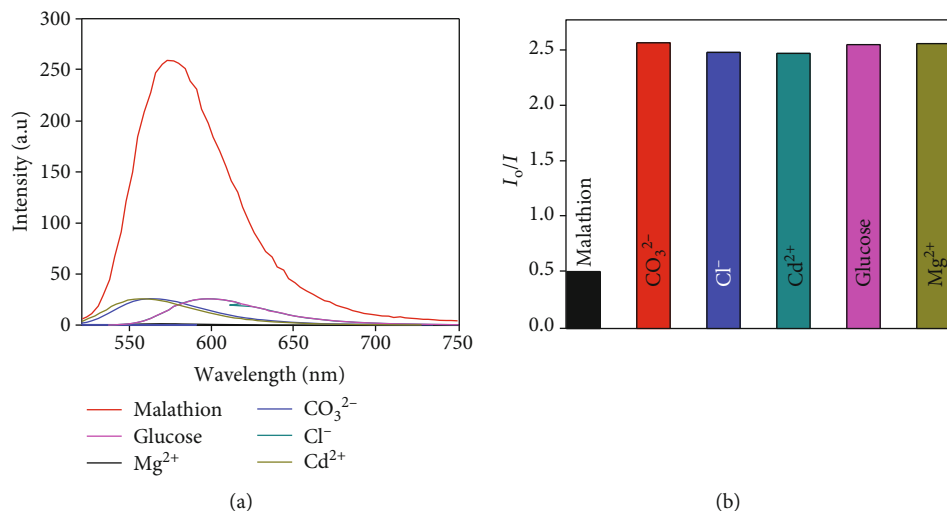
(a)

(b)

Figure 7: (a) The fluorescence intensity of Ag-ZnO/PANI NC with different interferences (Mg^{2+}, glucose, CO_3^{2-}, Cl^-, and Cd^{2+}, all interference concentrations of $0.125\,\mu M$) and MA ($0.5\,\mu M$) as the Ag-ZnO/PANI NC as control and (b) UV-vis spectral variation of Ag-ZnO/PANI NC upon additions of various OPs.

Table 1: Determination of MA spiked in commercial samples.

Sample ($n = 5$)	Spiked (μM)	Found ($\mu M/\mu g/L$)	Recovery (%)	RSD (%)
	0	0	0	0
	0.05	0.041	82	2.63
Potato	0.1	0.093	93	2.74
	0.15	0.11	96	1.32
	0.25	0.189	93.3	2.87
	0	0	0	0
	0.05	0.043	86	2.45
Tomato	0.1	0.089	89	3.11
	0.15	0.109	72	1.41
	0.25	0.179	71.6	1.93

RSD: relative standard deviation.

$0.8\,\mu M$ ($R^2 = 0.987$) as shown in Figures 6(c) and 6(d), respectively. This shows that the quantitative measurement of MA using Ag-ZnO/PANI NCs sensor can be accomplished with different sensitivities (slopes of the lines) of 1.022 and $0.0133\,\mu M$ according to the range of detection. The limit of detection acquired from the calibration line is $0.0081\,\mu M$ (Figure 6(b)). It is found that the NC has a reasonable limit of detection for MA; therefore, the result indicates the NC was sensitive enough to monitor MA concentration.

To check the selectivity performance of the sensor towards MA detection, a similar experiment was performed with different interference such as Mg^{2+}, glucose, CO_3^{2-}, Cl^-, and Cd^{2+} Figure 7(a) using a fluorescence spectrophotometer. The shape and band maxima of the fluorescence spectra remain unchanged, and no other emission towards longer wavelengths was noticed except for the redshift (~19 nm) of glucose due to interaction with NCs. This observation

suggests that the weak fluorophore–quencher interaction does not change the spectral of NCs.

The NC also showed high selectivity on UV-vis spectra Figure 7(b). Apart from MA, no other ion-induced absorption maximum shift. Furthermore, the interference investigation of these OPs indicated the NC was capable to be applied to complex environments with small interference from other ions. Hence, the fabricated sensor is quite selective and specific towards OPs on both fluorescence and UV-vis spectra.

3.5. Analysis of MA in Real Samples. The pretreated potato and tomato were added into Ag-ZnO/PANI, and the data were collected by a fluorescence spectrophotometer, and a calibration curve was used to study the spiked experiments. The results of the experiment are given in Table 1. Four samples were not detected in the absence of spiked MA, and those recovered were in the range of 91.0–99.6% and

TABLE 2: Comparison of performance of different MA probing methods.

Fluorescent probe	LOD (detection range)	Recovery (%)	Reference
TPCA-β-Cyclodextrin @AgNPs	0.01 μg/mL (0.1-25 μg/mL)	83-101	[10]
Eu(III)–Bathophenanthroline	0.92 mM	—	[11]
Magnetic-assisted FAM-apt	5.48 μg/mL	109.6	[12]
Apta-LFB with quantum dots nanobeads and Au nanostars	2.24 nM	—	[45]
Apt-AuNPs	4 pM (10 pM-1 μM)		[46]
Apt-SERS	500 nM-10 μM		[47]
Ag-ZnO/PANI	0.132 μM	92.0–99%	This work

LOD: limit of detection.

92.8–95.6% with acceptable results. The relative standard deviation (RSD) ranges were 1.19–5.05% and 4.01–5.06%, respectively. The sensitivity and selectivity of this method were comparable with most of the informed methods. A comparison between this work and other reported systems for MA sensing in detection limit (LOD) or linear range is summarized in Table 2.

4. Conclusion

In summary, a novel ultrasensitive fluorescence quenching probe based on Ag-ZnO/PANI NC was developed for MA detection, which has a detection limit of 0.132 μM. The fluorescence of Ag-ZnO/PANI NC is strongly quenched by MA and has several uses such as fast response time, good stability, high selectivity, and sensitivity. Additionally, the Ag-ZnO/PANI NC has been effectively used for MA detection in agricultural products with suitable results.

Data Availability

No data were used to support this study.

Conflicts of Interest

All authors declare that they have no conflict(s) of interest.

Acknowledgments

References

[1] R. Bala, A. Swami, I. Tabujew, K. Peneva, N. Wangoo, and R. K. Sharma, "Ultra-sensitive detection of malathion using quantum dots-polymer based fluorescence aptasensor," *Biosensors and Bioelectronics*, vol. 104, pp. 45–49, 2018.

[2] Q. Lang, L. Han, C. Hou, F. Wang, and A. Liu, "A sensitive acetylcholinesterase biosensor based on gold nanorods modified electrode for detection of organophosphate pesticide," *Talanta*, vol. 156, pp. 34–41, 2016.

[3] N. I. Valente, S. Tarelho, A. L. Castro, A. Silvestre, and H. M. Teixeira, "Analysis of organophosphorus pesticides in whole blood by GC-MS-μECD with forensic purposes," *Journal of Forensic and Legal Medicine*, vol. 33, pp. 28–34, 2015.

[4] Q. Chen, R. Sheng, P. Wang et al., "Ultra-sensitive detection of malathion residues using FRET-based upconversion fluorescence sensor in food," *Spectrochimica Acta Part A: Molecular and Biomolecular Spectroscopy*, vol. 241, article 118654, 2020.

[5] R. S. Chouhan, A. C. Vinayaka, and M. S. Thakur, "Thiol-stabilized luminescent CdTe quantum dot as biological fluorescent probe for sensitive detection of methyl parathion by a fluoroimmunochromatographic technique," *Analytical and Bioanalytical Chemistry*, vol. 397, no. 4, pp. 1467–1475, 2010.

[6] C. C. Leandro, P. Hancock, R. J. Fussell, and B. J. Keely, "Comparison of ultra-performance liquid chromatography and high-performance liquid chromatography for the determination of priority pesticides in baby foods by tandem quadrupole mass spectrometry," *Journal of Chromatography A*, vol. 1103, no. 1, pp. 94–101, 2006.

[7] X. Zhao, W. Kong, J. Wei, and M. Yang, "Gas chromatography with flame photometric detection of 31 organophosphorus pesticide residues in *Alpinia oxyphylla* dried fruits," *Food Chemistry*, vol. 162, pp. 270–276, 2014.

[8] M. Wei, J. J. S. Wang, and A. B. Chemical, "A novel acetylcholinesterase biosensor based on ionic liquids-AuNPs-porous carbon composite matrix for detection of organophosphate pesticides," *Sensors and Actuators B: Chemical*, vol. 211, pp. 290–296, 2015.

[9] T. Kohzadi, M. J. W. S. Roushani, and T. W. Supply, "Highly sensitive colorimetric determination of malathion using gold nanoparticles," *Water Science and Technology: Water Supply*, vol. 16, no. 5, pp. 1214–1220, 2016.

[10] M. Wang, K. Su, J. Cao et al., ""Off-On" non-enzymatic sensor for malathion detection based on fluorescence resonance energy transfer between β and fluorescent probe," *Talanta*, vol. 192, pp. 295–300, 2019.

[11] H. A. Azab, A. S. Orabi, and A. M. Abbas, "New probe for fluorescence detection of *azinphous ethyl*, *malathion* and *heptachlor* pesticides," *Journal of Luminescence*, vol. 160, pp. 181–187, 2015.

[12] M. Jiang, C. Chen, J. He, H. Zhang, and Z. Xu, "Fluorescence assay for three organophosphorus pesticides in agricultural products based on magnetic-assisted fluorescence labeling aptamer probe," *Food Chemistry*, vol. 307, article 125534, 2020.

[13] T. J. Dale and J. Rebek, "Fluorescent sensors for organophosphorus nerve agent mimics," *Journal of the American Chemical Society*, vol. 128, no. 14, pp. 4500-4501, 2006.

[14] Y. Hou, A. M. Soleimanpour, and A. H. Jayatissa, "Low resistive aluminum doped nanocrystalline zinc oxide for reducing gas sensor application via sol–gel process," *Sensors and Actuators B: Chemical*, vol. 177, pp. 761–769, 2013.

[15] Y. Xie, Y. Yu, L. Lu et al., "CuO nanoparticles decorated 3D graphene nanocomposite as non-enzymatic electrochemical sensing platform for malathion detection," *Journal of Electroanalytical Chemistry*, vol. 812, pp. 82–89, 2018.

[16] C. Bignon, S. Amigoni, T. Devers, and F. Guittard, "Barrier cream based on CeO_2 nanoparticles grafted polymer as an active compound against the penetration of organophosphates," *Chemico-Biological Interactions*, vol. 267, pp. 17–24, 2017.

[17] W. Wei, S. Dong, G. Huang, Q. Xie, and T. Huang, "MOF-derived Fe_2O_3 nanoparticle embedded in porous carbon as electrode materials for two enzyme-based biosensors," *Sensors and Actuators B: Chemical*, vol. 260, pp. 189–197, 2018.

[18] X. Yan, Y. Song, C. Zhu et al., "MnO_2 nanosheet-carbon dots sensing platform for sensitive detection of organophosphorus pesticides," *Analytical Chemistry*, vol. 90, no. 4, pp. 2618–2624, 2018.

[19] D. Zhang, N. Yin, and B. Xia, "Facile fabrication of ZnO nanocrystalline-modified graphene hybrid nanocomposite toward methane gas sensing application," *Journal of Materials Science: Materials in Electronics*, vol. 26, no. 8, pp. 5937–5945, 2015.

[20] H. Tian, H. Fan, H. Guo, and N. Song, "Solution-based synthesis of ZnO/carbon nanostructures by chemical coupling for high performance gas sensors," *Sensors and Actuators B: Chemical*, vol. 195, pp. 132–139, 2014.

[21] A. I. Uddin, D. T. Phan, and G. S. Chung, "Low temperature acetylene gas sensor based on Ag nanoparticles-loaded ZnO-reduced graphene oxide hybrid," *Sensors and Actuators B: Chemical*, vol. 207, pp. 362–369, 2015.

[22] V. Gilja, I. Vrban, V. Mandić, M. Žic, and Z. Hrnjak-Murgić, "Preparation of a PANI/ZnO composite for efficient photocatalytic degradation of acid blue," *Polymers*, vol. 10, no. 9, p. 940, 2018.

[23] W. K. Jo and N. C. Selvam, "Enhanced visible light-driven photocatalytic performance of ZnO–g-C_3N_4 coupled with graphene oxide as a novel ternary nanocomposite," *Journal of Hazardous Materials*, vol. 299, pp. 462–470, 2015.

[24] A. I. Uddin, U. Yaqoob, D. T. Phan, and G. S. Chung, "A novel flexible acetylene gas sensor based on PI/PTFE-supported Ag-loaded vertical ZnO nanorods array," *Sensors and Actuators B: Chemical*, vol. 222, pp. 536–543, 2016.

[25] B. Hatamluyi, Z. Eshaghi, F. M. Zahed, and M. Darroudi, "A novel electrochemical sensor based on GQDs-PANI/ZnO-NCs modified glassy carbon electrode for simultaneous determination of Irinotecan and 5-fluorouracil in biological samples," *Sensors and Actuators B: Chemical*, vol. 286, pp. 540–549, 2019.

[26] B. L. Martínez-Vargas, S. M. Durón-Torres, D. Bahena, J. L. Rodríguez-López, J. M. Peralta-Hernández, and A. Picos, "One-pot synthesis of ZnO-Ag and ZnO-Co nanohybrid materials for photocatalytic applications," *Journal of Physics and Chemistry of Solids*, vol. 135, article 109120, 2019.

[27] H. Tai, Y. Jiang, G. Xie, J. Yu, X. Chen, and Z. Ying, "Influence of polymerization temperature on NH3 response of PANI/TiO2 thin film gas sensor," *Sensors and Actuators B: Chemical*, vol. 129, no. 1, pp. 319–326, 2008.

[28] T. Chitradevi, A. J. Lenus, and N. V. Jaya, "Structure, morphology and luminescence properties of sol-gel method synthesized pure and Ag-doped ZnO nanoparticles," *Materials Research Express*, vol. 7, no. 1, article 015011, 2020.

[29] M. F. Nsib, S. Saafi, A. Rayes, N. Moussa, and A. Houas, "Enhanced photocatalytic performance of Ni-ZnO/polyaniline composite for the visible-light driven hydrogen generation," *Journal of the Energy Institute*, vol. 89, no. 4, pp. 694–703, 2016.

[30] F. Habtamu, S. Berhanu, and T. Mender, "Polyaniline supported Ag-doped ZnO nanocomposite: synthesis, characterization, and kinetics study for photocatalytic degradation of malachite green," *Journal of Chemistry*, vol. 2021, 12 pages, 2021.

[31] S. Ebrahim, A. Shokry, M. M. A. Khalil, H. Ibrahim, and M. Soliman, "Polyaniline/Ag nanoparticles/graphene oxide nanocomposite fluorescent sensor for recognition of chromium (VI) ions," *Scientific Reports*, vol. 10, no. 1, pp. 1–11, 2020.

[32] X. Hua, L. Wang, G. Li, Q. Fang, M. Wang, and F. Liu, "Multi-analyte enzyme-linked immunosorbent assay for organophosphorus pesticides and neonicotinoid insecticides using a bispecific monoclonal antibody," *Analytical Methods*, vol. 5, no. 6, pp. 1556–1563, 2013.

[33] X. Yan, H. Li, X. Wang, and X. Su, "A novel fluorescence probing strategy for the determination of parathion- methyl," *Talanta*, vol. 131, pp. 88–94, 2015.

[34] S. Mehrizi and M. H. Sohi, "Electrical resistivity and magnetic properties of electrodeposited nanocrystalline CoFe thin films," *Journal of Materials Science: Materials in Electronics*, vol. 26, no. 10, pp. 7381–7389, 2015.

[35] Y. Hou, J. Feng, Y. Wang, and L. Li, "Enhanced antibacterial activity of Ag-doped ZnO/polyaniline nanocomposites," *Journal of Materials Science: Materials in Electronics*, vol. 27, no. 7, pp. 6615–6622, 2016.

[36] K. Takahashi and T. Morizumi, "Growth of InAs whiskers in wurtzite structure," *Japanese Journal of Applied Physics*, vol. 5, no. 8, pp. 657–662, 1966.

[37] A. Shokry, M. M. A. Khalil, H. Ibrahim, M. Soliman, and S. Ebrahim, "Highly luminescent ternary nanocomposite of polyaniline, silver nanoparticles and graphene oxide quantum dots," *Scientific Reports*, vol. 9, no. 1, pp. 1–12, 2019.

[38] M. M. Rahman, A. Khan, H. M. Marwani, and A. M. Asiri, "Hydrazine sensor based on silver nanoparticle-decorated polyaniline tungstophosphate nanocomposite for use in environmental remediation," *Microchimica Acta*, vol. 183, no. 5, pp. 1787–1796, 2016.

[39] M. Mitra, A. Ghosh, A. Mondal, K. Kargupta, S. Ganguly, and D. Banerjee, "Facile synthesis of aluminium doped zinc oxide-polyaniline hybrids for photoluminescence and enhanced visible-light assisted photo-degradation of organic contaminants," *Applied Surface Science*, vol. 402, pp. 418–428, 2017.

[40] S. Poyraz, I. Cerkez, T. S. Huang et al., "One-step synthesis and characterization of polyaniline nanofiber/silver nanoparticle composite networks as antibacterial agents," *ACS Applied Materials & Interfaces*, vol. 6, no. 22, pp. 20025–20034, 2014.

[41] S. C. Ortiz, E. M. Ospino, and R. Cabanzo, "Spectroscopy characterization and quantum yield determination of quantum dots," *Journal of Physics: Conference Series*, vol. 687, no. 1, article 012097, 2016.

[42] J. El Nady, M. Ali, O. A. Kamel, S. Ebrahim, and M. Soliman, "Room temperature synthesis of aqueous ZnCuInS/ZnS quantum dots," *Journal of Dispersion Science and Technology*, vol. 41, no. 13, pp. 1956–1962, 2020.

[43] E. P. Kirby and R. F. Steiner, "Influence of solvent and temperature upon the fluorescence of indole derivatives," *The Journal of Physical Chemistry*, vol. 74, no. 26, pp. 4480–4490, 1970.

[44] M. Afshari, M. Dinari, and M. M. Momeni, "The graphitic carbon nitride/polyaniline/silver nanocomposites as a potential electrocatalyst for hydrazine detection," *Journal of Electroanalytical Chemistry*, vol. 833, pp. 9–16, 2019.

[45] N. Cheng, Y. Song, Q. Fu et al., "Aptasensor based on fluorophore-quencher nano-pair and smartphone spectrum reader for on-site quantification of multi-pesticides," *Biosensors and Bioelectronics*, vol. 117, pp. 75–83, 2018.

[46] R. Bala, R. K. Sharma, and N. Wangoo, "Development of gold nanoparticles-based aptasensor for the colorimetric detection of organophosphorus pesticide phorate," *Analytical and Bioanalytical Chemistry*, vol. 408, no. 1, pp. 333–338, 2016.

[47] Y. Nie, Y. Teng, P. Li, W. Liu, Q. Shi, and Y. Zhang, "Label-free aptamer-based sensor for specific detection of malathion residues by surface-enhanced Raman scattering," *Spectrochimica Acta Part A: Molecular and Biomolecular Spectroscopy*, vol. 191, pp. 271–276, 2018.